07,08,09

Transmission Electron Microscopy of Crystallization Process of Amorphous Iron Oxide Films

© A.M. Murzakaev

Institute of Electrophysics, Ural Branch, Russian Academy of Sciences,
Yekaterinburg, Russia

E-mail: amurzak@mail.ru

Received April 23, 2025
Revised May 20, 2025
Accepted May 27, 2025

Crystal growth in amorphous thin iron oxide films is accompanied by the formation of transrotational crystals. The aim of this work is to identify the growth mechanism of transrotational crystals. Crystal growth and the structure of crystallized regions in amorphous thin Fe_2O_3 films were studied in situ using a transmission electron microscope (TEM). Structural changes were revealed by electron diffraction methods (selected area electron diffraction — SAED). High-resolution transmission electron microscopy (HRTEM) studies revealed oxygen vacancies in Fe_2O_3 samples. They are arranged by forming crystallographic shear planes (CS). Processing and analysis of HRTEM images revealed a large number of dislocations and disclinations. All types of crystal lattice defects revealed by HRTEM, and especially dislocations with disclinations, can contribute to the formation (emergence) of a transrotational crystal lattice.

Keywords: Amorphous films, transrotational crystal, HRTEM, crystallographic shear, stacking faults, dislocation, disclination.

DOI: 10.61011/PSS.2025.05.61498.91-25

1. Introduction

In the last decades the number of iron oxide-based nanomaterials have been studied increasingly. In the systems of information recording and storage the crystallization of amorphous iron oxide films is of interest from the practical and scientific points of view. When a thin amorphous iron oxide film is subjected to any method (laser, electron beam, heating), transrotational crystals may be formed. Initially they were found when crystals grow in amorphous films of chalcogenides (Se, Se-Te, Cu-Te) [1] in a transmission electron microscope (TEM) using annealing *in situ*. According to the data of paper [2], the presence of multiple bending contours in the case of crystallizing thin films Fe_2O_3 indicates an internal bend of a crystalline lattice called transrotational. Were observed no features in the patterns of high-resolution transmission electron microscopy (HRTEM), in the center of transrotational nucleating seeds, where an unusual event originates, or in the front of crystallization at the periphery of the growing crystal. Neither the spectra of energy-dispersive X-ray spectroscopy (EDX), nor the characteristic electron energy losses spectra (EELS) showed no difference in the composition that could be related to the unusual rotation of the lattice orientation. Neither inclusions of amorphous material, nor dislocations were observed inside the transrotational crystalline areas. Regular permanent internal bend of the lattice manifests as a non-changing electron diffraction analysis pattern (selected area electron diffraction — SAED) at specimen inclination tilting in TEM. In paper [3] the atomic-force microscopy method was used to demonstrate that the observed crystallites α-Fe_2O_3 were practically flat: no crystal bend is observed in general. There is no systemic disturbance in the central region on the common relief. The amorphous film that surrounds the crystal is substantially bent by large folds with spread along the height (from a fold to a fold) up to 500 nm, which radially extend from the crystal. Such pattern is probably related to the stress and (or) redistribution of material in the amorphous matrix in the process of crystal origination and growth α-Fe_2O_3. The internal bend of the lattice may not be related to the features of a chemical bond, since it was found for substances of various chemical nature [3–16]. The special structure of transrotational crystals was found and studied in detail previously, but there is still no proper explanation of how this structure appears and exists. Paper [17] presents the explanation based on density increase, which occurs in process of amorphous-crystalline phase transformation. For a thin film, the density increases, in particular, perpendicularly to free surface, since only in this direction the shape change is unlimited. So, there is a trend towards bending of crystalline planes, but the additional requirement is that the material must be sensitive to the bending exposure. This is also related to the energy stability of the internally bent structure.

The purpose of this article is to explain the formation of transrotational crystallites in thin films Fe_2O_3 and to study structural and phase changes under the comparatively long-term exposure to electrons. In this paper transrotational crystallites were obtained in TEM *in situ*. To find out the mechanism for formation of transrotational crystals, a detailed analysis of SAED and HRTEM patterns obtained

in process of *in situ* crystallization of amorphous films. Besides, the recovery of iron oxide was studied under long-term exposure to the electron beam.

2. Materials and experimental methods

2.1. Manufacturing of thin films

Amorphous films of iron oxides were obtained by thermal oxidation of iron pentacarbonyl $Fe(CO)_5$ on the freshly cleaved (in air) NaCl single crystals as a substrate. The studied films were separated from the substrate in distilled water and placed on the copper lattices for electron microscopy.

2.2. Crystallization with electron beam

Crystallization was initiated by the action of the focused electron beam inside the used TEM. This made it possible to track the phase transformation *in situ*. Electron radiation of amorphous films was done with electron beam focusing at round areas with diameter from 20 to 200 nm depending on the size of the studied nanostructure. The beam intensity was supported permanent due to variation of radiation time and electron dose depending on the areas illuminated with the beam. Effects caused by exposure of the electron beam were controlled by recording of TEM images at different radiation time. To prevent further growth of crystals, the studies of their structure were conducted at the minimum possible beam intensity.

2.3. Structural studies

TEM analysis was carried out using JEOL JEM 2100 at accelerating voltage of 200 kV. Spherical aberration coefficient C_s is 0.5 mm. Spatial resolution of this device is 0.14 nm along the lines and 0.19 nm along the dots. Calibration of HRTEM magnification and determination of the device constant for electron diffraction measurements were performed using gold foil. Error of interplanar spacing measurement is ± 0.01 nm. Effects caused by exposure of the electron beam were controlled by recording of TEM images at various radiation time. Serial changes of the specimen structure were studied using analysis of SAED and HRTERM images. Processing and analysis of HRTEM images were carried out using Gatan Digital Micrograph (DM) software, version 3.9.3, which made it possible to calibrate images, apply masks and filters, do fast Fourier transforms (FFT) of the entire image and its selected areas, to do measurements. Values of interplanar spacings to determine phase composition were taken from the powder diffraction database (PDF files). Thin films were homogeneous on the substrates. The chemical composition was analyzed by method of X-ray energy-dispersive spectroscopy, and the results have shown that the films had stoichiometric composition. The films had even amorphous contrast without any signs of even fine particles or lattice bands, which makes it possible to assume that all specimens were fully amorphous prior to exposure to the focused electron beam.

3. Results and discussion

3.1. Features of crystal structure

3.1.1. TEM and SAED observations

Areas of the amorphous film radiated with electrons are crystallized after a certain latent period of time. Crystallization starts with formation of a nucleating seed. The crystallite formation time is from 1 to 10 min for intermediate intensities and depends on the film thickness. In thinner films the crystallization is faster. Figure 1 shows a specific TEM pattern of the crystallized area of the studied specimen Fe_2O_3. Insert *1* shows an electron diffraction pattern demonstrating a diffuse pattern of electron diffraction obtained at the initial moment of electron beam exposure, which confirms the initially amorphous nature of the specimen. Insert *2* is a SAED pattern obtained in the central area of the crystal, showing clear diffraction spots and indicating the single-crystal nature of the crystal. When the specimens were inclined in SAED mode, the diffraction spot positions did not change. Using a holder of specimens with double tilting it was also demonstrated that this curvature is present for any axis of inclination in the film plane. Therefore, the observed growth formation is a crystal that is continuously bent. The bend contours are the internal property of the crystal, and not the artifact of the specimen preparation, such as the bend of the film itself [2]. Such objects are formed in thin (< 100 nm) amorphous films and are therefore flat. Interpretation of SAED patterns yielded the following result: the crystals have a rhombohedral crystalline structure — hematite α-Fe_2O_3 (JCPDS PDF 01-088-2359, hereinafter we will only specify a nine-digit number from the database).

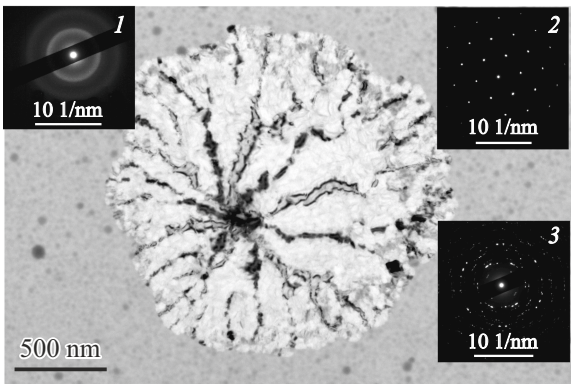

Figure 1. TEM pattern of crystallized area *in situ* Fe_2O_3 in amorphous film. (Description of the inserts is provided in the text).

3.1.2. HRTEM observation

Figure 2 presents an HRTEM image of the central region of transrotational crystal Fe_2O_3. At first sight, according to SAED (insert *2* in Figure 1) in the center of the transrotational crystal (where it arose) it is perfect. Interpretation of bright and wide FFT points (insert in Figure 2) yielded the value of interplanar spacings at 0.255 nm (01-088-2359). However, the analysis of HRTEM patterns in measurement of interplanar spacings (according to the intensity profile, the measurement area is specified on insert *b*, Figure 2) shows that there are changes in the interplanar spacings. It has turned out that the interplanar spacings, determined from the intensity profile (Figure 3) do not match the interplanar spacing value determined using FFT points. Spacing between the first and second layers $d_1 = 0.245$ nm. Spacing between the second and third layers $d_2 = 0.267$ nm. Spacings between the third and fourth, fourth and fifth layers are repeated as from the first to the third layer. Then the spacings d_1 and d_2 between the layers change randomly. The ten first layers have the thickness of 2.581 nm. The average interplanar spacing is 2.581 nm/10 = 0.2581 nm. The average interplanar spacing for 20 layers is 5.173 nm/20 = 0.25865 nm, and for 30 layers — 7.697 nm/30 = 0.2565 nm. It means that even the central part of the film has a defective structure. It follows from the iron oxide database that the interplanar spacing $d_2 = 0.267$ nm complies with rhombohedral structure Fe_2O_3 (01-084-0311), and interplanar spacing $d_1 = 0.245$ nm within the detection error may comply with the FeO rhombohedral structure (01-073-2145).

Application of masks on FFT (Fourier masking) may remove the unwanted noise and reinforce the periodical elements of the HRTEM image. Two types of HRTEM images processing were used: ring filtration and polar filtration. The first selects frequencies in the Fourier space around the first-order diffraction spots in the image

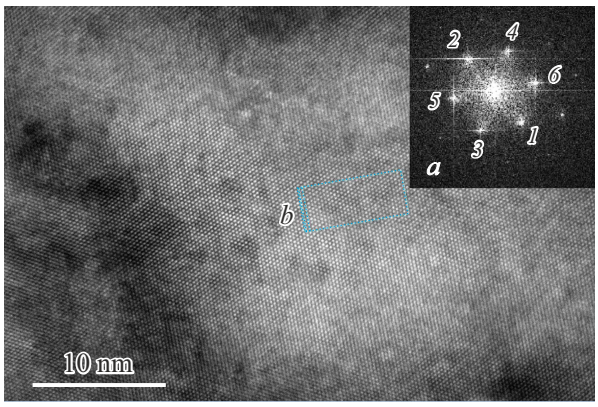

Figure 2. HRTEM image of the central area of transrotational crystallite Fe_2O_3. Inserts: *a* — corresponding to FFT, *b* — section identified with a rectangle — place of measurement of interplanar spacings according to the intensity profile.

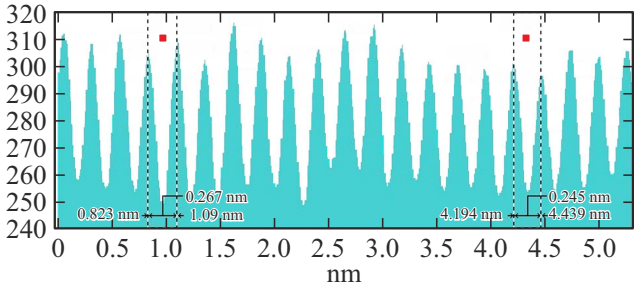

Figure 3. Intensity profile with interplanar spacings of the section identified with a rectangle *b* in Figure 2.

and removes most disturbances. Such processing does not displace the extremum position on the image. The second one localizes two symmetrical diffraction spots in the Fourier space to obtain the images of a single family of planes. Such processing will not exactly preserve precisely the extremum positions in the defect nucleus structures, but its advantage consists in the fact that it clearly shows the availability of dislocation or a planar defect.

Pairs of diametrally opposite points (1 and 2, 3 and 4, 5 and 6) were selected from FFT on insert *a* Figure 2, and based on these points, the structure images were reconstructed using inverse fast Fourier transform (IFFT). Detailed reconstruction of the image demonstrated that only on the basis of points 1 and 2 the crystalline structure is distorted (Figure 4, *a*). The circumference specifies the position of the dislocation nucleus. The image with IFFT reconstructed from the FFT image with ring filtration is shown in Figure 4, *b*. You can clearly see the dislocation of single capacity on this HRTEM image. Use of masks and filters on other HRTEM patterns made it possible to identify many dislocations. On thinner films the number (density) of dislocations is more compared to thicker films (Figure 4, *c*).

Using DM software, the crystalline lattice plane inclination angles were measured. The following results were shown in Figure 5 near dislocation (0° — bottom of the pattern from the left to the right): line *1* is inclined at angle $\varphi_1 = 40.10°$, and line *2* is inclined at angle $\varphi_2 = 40.75°$, $\Delta\varphi = 0.65°$. The crystalline lattice in the upper part relative to the lower part is turned by $\Delta\varphi = 0.65°$ due to disclination. Planes *3* and *4* have the following angle values: $\varphi_3 = -79.18°$, $\varphi_4 = -79.19°$, $\Delta\varphi = 0.01°$. Within the limits of the measurement errors, planes *3* and *4* may be deemed parallel.

3.2. Features of polycrystal structure

3.2.1. TEM and SAED observations

With further radial growth of the transrotational crystal to several microns the SAED (pattern with points (spots)) is transformed into a pattern with diffraction rings (with or

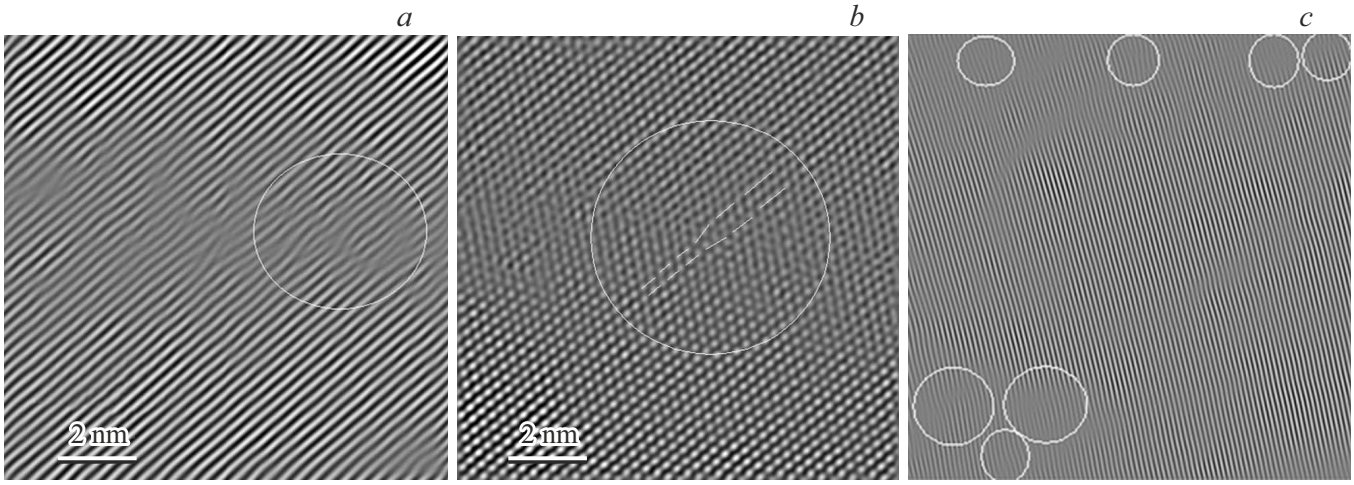

Figure 4. Patterns of dislocations obtained after polar filtration (a and c) and ring filtration (b) on transrotational iron oxide crystals.

without texture), specific for a polycrystalline film (insert *3* in Figure 1 and insert *2* in Figure 6). These electron diffraction patterns from polycrystalline areas comply with the rhombohedral structure α-Fe_2O_3 (01-088-2359), cubic structure of maghemite-C Fe_2O_3 (00-039-1346), orthorhombic structure of magnetite Fe_3O_4 (01-076-0958) and face-centered cubic (FCC) structure FeO (01-089-0687). Diameters of spots and width of circumferences in the SAED pattern are increased. The average size of crystallites is around 5 nm after 12 min of exposure and increases slightly to approximately 7 nm after 20 min of exposure. In general the dimensions of these crystallites are in the range from 3 to 20 nm. Under further radiation with electron beam the particle size will not increase significantly.

3.2.2. HRTEM observations

The phase composition may be determined from the analysis of HRTEM images in individual nanocrystals. Detailed studies were carried out for the structure and phase composition of a large quantity of nanoparticles formed after crystallization under long-term exposure to electron radiation. Based on the initial HRTEM pattern or the separated area of the pattern, we get a fast Fourier transform (FFT) pattern, which is equivalent to the electron diffraction pattern of the entire image or the selected area. Then the FFT pattern is analyzed, and interplanar spacings are determined. Figure 7, a presents the enlarged image of the separated area 3 from Figure 6. Interplanar spacing determined from FFT points 1 and 2 (insert in Figure 7, a), is 0.485 nm, and such spacing may comply with FCC structure Fe_3O_4 (01-074-1909). Interplanar spacing determined according to the intensity profile is 0.489 nm, within the limits of the experimental determination error (± 0.01 nm) matches the value of interplanar spacing determined by FFT points 1 and 2.

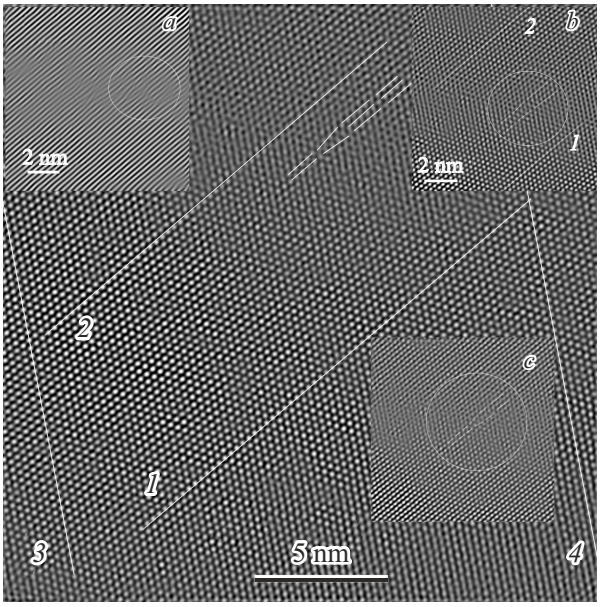

Figure 5. Pattern of transrotational crystal Fe_2O_3 demonstrating rotation of crystalline lattice due to disclination.

Figure 7, b presents the enlarged image of the separated area 4 in Figure 6. Interplanar spacing produced from FFT points 1 and 2 (on insert in Figure 7, b), makes 0.48 nm and is similar to data from Figure 7, a. However, the interplanar spacings, determined from the intensity profile do not match the interplanar spacing value determined using 1 and 2 FFT points. Spacing between the first and second layers $d_1 = 0.491$ nm. This interplanar spacing value may correspond to the magnetite structure Fe_3O_4 (01-089-0951). Spacing between the second and third layers $d_2 = 0.458$ nm. This interplanar spacing value may correspond to the magnetite structure Fe_3O_4 (01-089-0951). Then the spacings d_1 and d_2 between the layers change

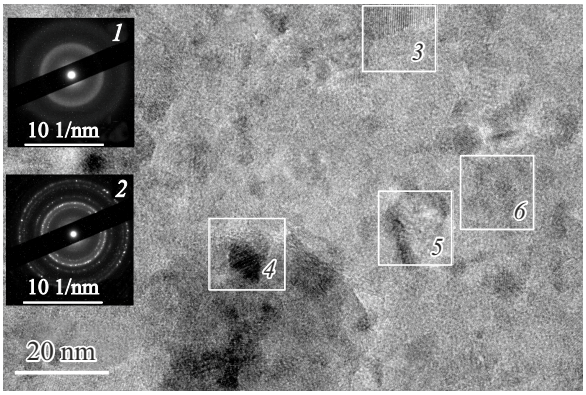

Figure 6. Crystallized *in situ* polycrystals in the film of the amorphous iron oxide.

randomly. In general the eight layers have thickness of 3.834 nm. Average interplanar spacing for 8 layers is $3.834/8 = 0.47925$ nm, within the limits of the experimental determination error (± 0.01 nm) matches the value of interplanar spacing determined by FFT points 1 and 2.

Figure 7, *c* presents the enlarged image of the separated area 5 in Figure 6. Interplanar spacing produced from FFT points 1 and 2 (on insert in Figure 7, *c*), makes 0.30 nm. This value of interplanar spacing may comply with orthorhombic structure Fe_2O_3 (00-047-1409), orthorhombic structure Fe_3O_4 (01-076-0955, -0957, -0958), FCC structure Fe_3O_4 (01-089-0951). Interplanar spacings, determined from the intensity profile do not match the interplanar spacing value determined using 1 and 2 FFT points. Spacing between the first and second layers $d_1 = 0.293$ nm. This value of interplanar spacing may comply with orthorhombic structure Fe_2O_3 (00-047-1409), orthorhombic structure Fe_3O_4 (01-076-0955, -0957, -0958), FCC structure Fe_3O_4 (01-089-0951). Spacing between the second and third layers $d_2 = 0.326$ nm. This value of interplanar spacing may comply with orthorhombic structure Fe_3O_4 (01-076-0955, -0957, -0958). Then the spacings d_1 and $d_2$between the layers change randomly. In total the ten first layers have the thickness of 3.032 nm. The average interplanar spacing for 10 layers is $3.032/10 = 0.3032$ nm, and for 20 layers — 6.031 nm$/20 = 0.301$ nm.

Figure 7, *d* presents the enlarged image of the separated area 6 in Figure 6. Interplanar spacing obtained from the FFT pattern (point 1–4) is 0.25 nm. This value of interplanar spacing may comply with α-Fe_2O_3 (01-084-0311), γ-Fe_2O_3 (00-013-0458), β-Fe_2O_3 (01-076-1821), FCC structure Fe_3O_4 (01-075-0449, 01-079-0418). Interplanar spacings determined from the intensity profile do not match the value of interplanar spacing determined using FFT points. Spacing (from the upper left edge of the crystal) between the first and second (also 2–3, 3–4, 4–5) layers $d_1 = 0.262$ nm. This value of interplanar spacing may comply with γ-Fe_2O_3 (00-013-0458), β-Fe_2O_3 (01-076-1821), orthorhombic structure Fe_3O_4 (01-076-0955, 01-076-0957, 01-089-6466, 99-206-4077, 99-206-4383). Spacing between the fifth and sixth layers $d_2 = 0.229$ nm. This value of interplanar spacing may comply with γ-Fe_2O_3 (00-013-0458), β-Fe_2O_3 (01-076-1821), orthorhombic structure Fe_2O_3 (00-047-1409), rhom-

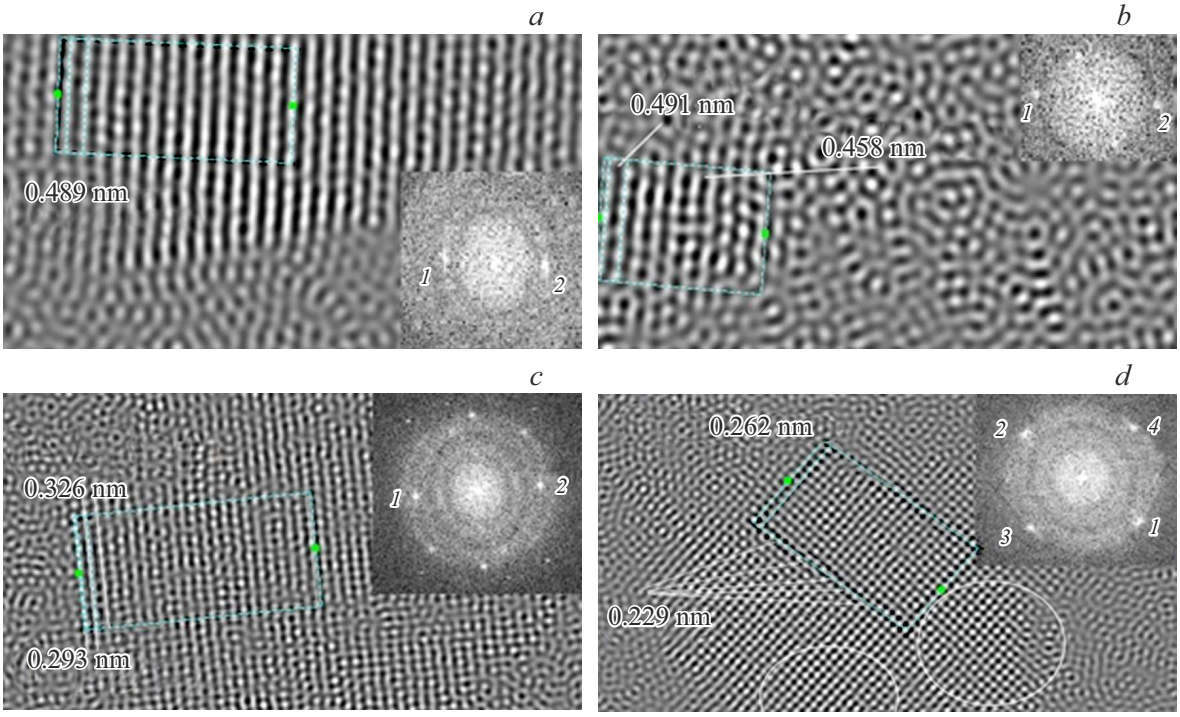

Figure 7. HRTEM-images of separated areas 3 (*a*), 4 (*b*), 5 (*c*) and 6 (*d*) in Figure 6.

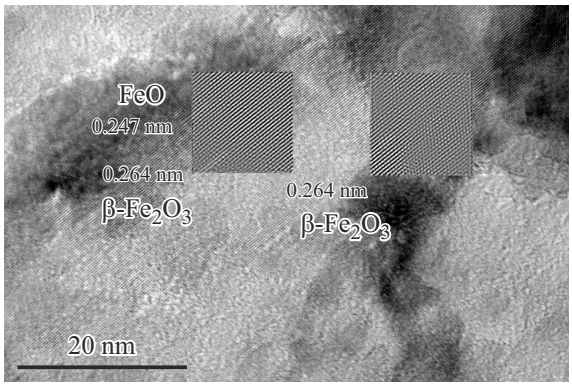

Figure 8. HRTEM of amorphous-crystalline boundary.

bohedral structure Fe_2O_3 (00-013-0534, 01-085-0599, 01-085-0987, 01-089-8103, 01-089-8104), orthorhombic structure Fe_3O_4 (01-076-0955, 01-076-0957, 01-089-6466). Spacings between the sixth and seventh layers are repeated, same as from the first to the second layer. Then the spacings d_1 and $d_2$between the layers change randomly. In total the twenty first layers have the thickness of 5.123 nm. The average interplanar spacing for 20 layers is $5.123/20 = 0.25615$ nm, and for 30 layers — $7.697\,\text{nm}/30 = 0.2565$ nm. Areas that contain only β-Fe_2O_3, are circled. Particle size β-Fe_2O_3, obtained in this study is around 5 nm. Particles without defects (with one and the same value of interplanar spacings) are very rare.

Figure 8 presents an HRTEM pattern of amorphous-crystalline boundary. The boundary between the amorphous material and crystallized area of around 1 nm, characterized by the intermediate ordering and change in the diffraction contrast. Amorphous areas are also observed in the crystallite environment.

3.3. Discussion

The spacings of the perfect crystal between parallel planes of the crystalline lattice and on the HRTEM patterns between individual bands (layers) must be strictly identical. Analysis of many HRTEM images Fe_2O_3 showed that all specimens contained defective structures. These defective structures Fe_2O_3 are very similar to the structure of nonstoichiometric oxides. Under the conditions of oxygen deficiency, the structural formation principles of phases of certain oxides were formulated by Magneli [18], Wadsley [19] and other researchers [20,21] who suggested the term „crystallographic shear" (CS) — an operation which leads to the formation of defects of a certain type. Oxides with oxygen deficit consist of regions with a perfect stoichiometric structure of oxide separated with planes of crystallographic shear (CS-planes), which are thin „lamellar" crystal regions with a different structure and composition. Oxygen deficiency present in the entire crystal „is concentrated" in these CS planes and they are arranged chaotically in the structure. You may state that after exposure to an electron beam the crystalline areas Fe_2O_3 on the amorphous film have the structure with additional FeO CS planes. Formation of these defects of the crystalline structure in small areas of the films produced by exposure to an electron beam may be related to sharply non-equilibrium conditions of their formation.

Paper [22] found structural changes induced by an electron beam in MoO_3 and MoO_{3-x} with the help of *in situ* TEM. MoO_3 nanostructures with orthorhombic structure were converted into a phase of Magneli oxide (c-Mo_4O_{11}) after 10 min radiation with an electron beam. Oxygen loss from the oxide caused structural changes. Structural changes were explained by local heating of the radiation area in combination with radiolysis. According to paper [23], formation of oxygen vacancies is enhanced by tension in oxides with several degrees of oxidation (Mn, Fe, Co, Ni, Cu). In paper [24] were observed that nanowires from Fe_2O_3 after recovery bent due to deformation. Deformation impacts the energy of formation of oxygen vacancies. Formation of modulated structures caused by long-range ordering of oxygen vacancies was also observed in papers [25–27]. As you know, Fe cations in the lattice α-Fe_2O_3 are located in octahedral points, the size of which is comparable to the size of Fe cation [28]. Electron bombardment in vacuum results in removal of oxygen anions from the lattice and increases Fe/O ratio. Therefore, some Fe cations are displaced to tetrahedral points, the size of which is much smaller than in octahedral points. To remove stress arising from lattice distortion, dislocations will be formed. HRTEM was used to identify disclinational dipoles in the mechanically ground nanocrystalline Fe [29]. It was found that these defects were present in nanogranular materials not only as a result of severe plastic deformation, but as a result of increased dependence on the intergranular sliding in process of deformation. Observation of disclinations in nanogranular materials confirms the hypothesis that nanogranular materials are deformed mostly through the grain boundary mechanisms and not dislocation sliding. For larger grains the elastic bend becomes less and less beneficial from the energy point of view. Disclinations are beneficial from the energy point of view for small disorientation angles.

In paper by V.Yu. Kolosov [2] it was determined that the electron beam intensity dictated the speed of crystal growth Fe_2O_3: the higher the intensity, the higher the crystal growth speed and the smaller the internal bend of the lattice. At lower intensities the crystal growth speed is lower, but the internal bend of the lattice was higher. We found that the crystals (located next to each other) formed with high intensity of the electron beam have smaller quantity (density) of dislocations, and the crystals formed at lower intensity of the electron beam have larger quantity (density) of dislocations. In paper [12] it was found that in thin antimony films (20−30 nm) the bend of the transrotational crystal lattice may reach 127 deg/μm, and in thicker films (60−70 nm) the lattice

bend was (12−17 deg/μm). We found that on thinner films the number (density) of dislocations is more compared to thicker films.

Plastic deformation of the studied materials Fe_2O_3 may occur due to increase of the density that happens in amorphous-crystalline phase conversion and movement of dislocations and disclinations. HRTEM found individual dislocations, which make up partial disclinations in nanocrystalline Fe_2O_3, which were subjected to severe plastic deformation in process of crystallization when exposed to the electron beam.

Formation and migration of disclinations for the time of deformation fragments and rotates nanocrystals. Such readjustments are important and critical processes happening in process of material deformation and, accordingly, may be decisive in formation of nanocrystalline materials and in heating, as well as in other deformation processes. Deformation readjustments under the exposure to the electron beam with formation of nanocrystals with the defective structure are important basic phenomena that may contribute to formation of transrotational crystals.

Small-angle grain boundary consists of a periodical array of dislocations, and is useful for design and composition of transrotational crystalline structures. Small-angle grain boundary is defined as the boundary between two crystalline grains with disorientation of usually less than 2°. Disorientations of small-angle grain boundary are compensated by the presence of dislocations. Small-angle grain boundaries are divided into two types: inclination and twisting boundaries. Mostly the small-angle inclination boundary consists of an array of edge dislocations with Burgers vector perpendicular to the plane of the boundary, and the direction of the line parallel to the axis of rotation, whereas the small-angle twisting boundary consists of a network of helical dislocations with Burgers vector on the boundary plane. Screw dislocation is not observed in HRTEM. In our turn, we may compose various transrotational crystalline structures, artificially creating dislocations and small-angle grain boundaries.

Schematic illustration of the mechanism responsible for the internal bend of the crystalline lattice, in transrotational crystals may be the following:

– crystalline planes move as mostly unbent into the amorphous matrix;

– new crystalline plane(s) form(s) on the surface. Due to the difference in the specific volume, the crystallite surface is at the lower height (level) compared to the amorphous environment;

– with further movement of the crystal/amorphous substance boundary, shrinkage occurs related to the transformation, which causes bending impact on the moving crystalline planes;

– plastic deformation of the materials occurs due to increase of the density that happens in amorphous-crystalline phase conversion and movement of dislocations and disclinations;

– dislocations and disclinations start rotating the crystal and therefore form a transrotational crystal.

Another quite interesting note may be added to the obtained results. To enhance the efficiency of absorption and reflection of the microwaves in composites, dielectric and magnetic nanoscale fillers are used together with carbon fibers, either separately or in a combination. Iron oxide ferrites are used as magnetic fillers due to their higher permittivity, stronger magnetization of saturation and improved resistance to the depth of the skin layer at high frequencies of the electromagnetic range [30]. Nanoscale flakes α-Fe_2O_3 [31], dendritic γ-Fe_2O_3 and dendritic Fe_3O_4 have the most attractive characteristics, too [32]. But long-term use of these materials in aerospace equipment is complicated. This is due to the fact that external conditions are characterized by extremely low oxygen content and presence of radiation with high energy particles. All of this may result in recovery of iron oxide and loss of magnetic properties. Recovery mechanisms in the FexOy systems remain unstudied to a large extent, therefore specifying the limit for wider engineering applications. TEM is an effective method to study the dynamic microstructural evolution of the materials exposed to high energy electron radiation in vacuum. The obtained results in this paper may provide answers to some questions. However, the knowledge in the atomic scale regarding the radiation in vacuum or effects of size at recovery reactions in Fe−O compounds are far from development.

4. Conclusions

Thus, the following conclusions can be made based on the study results. Analysis of HRTEM images showed that at the level of micro- and nanoscale.

1. There are inhomogeneities of chemical composition and various defects in the structure of crystals, which may not be found (detected) using X-ray diffraction analysis, electron diffraction analysis of the identified areas due to wider peaks and spectra of EDX or EELS due to low spatial resolution.

2. In Fe_2O_3 crystals due to nonstoichiometry the defects are formed in the crystal structure with the crystallographic shear type. Wadsley defects are found (chaotically distributed crystallographic shear planes in the normal packing).

3. All Fe_2O_3 crystals have multiple dislocations. All these dislocations indicate directed expansion of crystallites. The small-angle grain boundary consists of an array of dislocations.

4. The general interpretation of the fact that orientation of crystals inside a transrotational crystal may be single-crystal is not consistent with the reality. Microphotographs have shown that transrotational crystals are always polycrystalline with high degree of defects.

As a result of completed studies, a model of transrotational crystals formation was proposed.

Acknowledgments

The study was conducted in the equipment of the Collective Use Center, Institute of Electrophysics, Ural Branch of the Russian Academy of Sciences.

Funding

This study was supported by the Russian Foundation for Basic Research with grant (20-02-00906 A) and was conducted within state assignment 125020601676-4.

Conflict of interest

The author declares that he has no conflict of interest.

References

[1] I.E. Bolotov, V.Yu. Kolosov, A.V. Kozhyn. Phys. Status Solidi A **72**, 645 (1982).
[2] V.Yu. Kolosov, A.R. Thölén. Acta Mater. **48**, *8*, 1829 (2000).
[3] V.Yu. Kolosov, K.L. Shvamm, R.V. Gaynutdinov, A.L. Tolstikhina. Izv. RAN, ser. Fizicheskaya **71**, *10*, 1481 (2007). (in Russian).
[4] A.G. Bagmut, V.A. Zhuchkov, V.Yu. Kolosov, V.M. Kozevich, D.V. Melnichenko. Kristallografiya **51**, 150 (2005). (in Russian).
[5] V.Yu. Kolosov, L.M. Veretennikov, Yu.B. Startseva, K.L. Shvamm. FTP **39**, *8*, 990 (2005). (in Russian).
[6] A.G. Bagmut, S.N. Grigorov, V.A. Zhuchkov, V.Yu. Kolosov, V.M. Kozevich, D.V. Melnichenko. Izvestiya vuzov. Fizika **50**, *11*, 5 (2007). (in Russian).
[7] V.Yu. Kolosov, C.L. Schwamm, J.W. Steeds. J. Phys. Conf. Ser. **100**, 082038 (2008).
[8] V.Yu. Kolosov, A.V. Kozhin, L.M. Veretennikov, C.L. Schwamm. 14th European Microscopy Congress 343 (2008).
[9] V.Yu. Kolosov, A.A. Yushkov, L.M. Veretennikov. J. Phys.: Conf. Series **1115**, 032087 (2018).
[10] V.Yu. Kolosov, A.A. Yushkov. AIP Conf. Proceed. **2313**, 030019 (2020).
[11] A.A. Yushkov, V.Yu. Kolosov. Chimica Techno Acta **10**, *1*, 6480 (2023).
[12] V.Yu. Kolosov, A.A. Yushkov, L.M. Veretennikov, A.O. Bokunyaeva. ZhTF **92**, 1727 (2022). (in Russian).
[13] A. Alberti, C. Bongiorno, B. Cafra, G. Mannino, E. Rimini, T. Metzger, C. Mocuta, T. Kamler, T. Feudel. Acta Crystallogr. Sect. B: Struct. Sci. **61**, 486 (2005).
[14] A. Alberti, C. Bongiorno, P. Alippi, A. La Magna, C. Spinella, E. Rimini. Acta Crystallogr., Sect. B: Struct. Sci., B **62**, 729 (2006).
[15] A. Alberti, C. Bongiorno, E. Rimini, M.G. Grimaldi. Appl. Phys. Lett. **89**, 102105 (2006).
[16] J.A. Kalb, C.Y. Wen, Frans Spaepen, H. Dieker, M. Wuttig. J. Appl. Phys. **98**, 054902 (2005).
[17] B.J. Kooi, J.Th.M. De Hosson. J. Appl. Phys. **95**, 4714 (2004).
[18] J.S. Andersson, B. Collén, U. Kuylenstierna, A. Magnéli. Acta Chem. Scand. **11**, 1641 (1957).
[19] A.D. Wadsley. In: Organic Chemistry. Non-stoichiometric compounds Academic Press, N.Y. (1964). P. 98–209.
[20] J.S. Anderson. In: Modern Aspects of Solid State Chemistry / Ed. C.N.R. Rao. Springer New York, N.Y. (1970). P. 29–105.
[21] D.E. Diaz-Droguett, A. Zuniga, G. Solorzano, V.M. Fuenzalida, J. Nanopart. Res. **14**, 679 (2012).
[22] U. Aschauer, R. Pfenninger, S.M. Selbach, T. Grande, N.A. Spaldin. Phys. Rev. B **88**, *3*, 054111 (2013).
[23] W. Zhu, J. Winterstein, I. Maimon, Q. Yin, L. Yuan, A.N. Kolmogorov, R. Sharma, G. Zhou. J. Phys. Chem. C Nanomater. Interfaces **120**, *27*, 14854 (2016).
[24] Z.Q. Chen, U. Cvelbar, M. Mozetic, M.K. Sunkara, M.K. Chem. Chem. Mat. **20**, *9*, 3224 (2008).
[25] U. Cvelbar, Z.Q. Chen, M.K. Sunkara, M. Mozetic. Small **4**, 1610 (2008).
[26] A. Nasibulin, S. Rackauskas, H. Jiang, Y. Tian, P. Mudimela, S. Shandakov, L. Nasibulina, S. Jani, E. Kauppinen. Nano Res. **2**, 373 (2009).
[27] Y.C. Lee, Y.Y.L. Chueh, C.H. Hsieh, M.T. Chang, L.J. Chou, Z.L. Wang, Y.W. Lan, C.D. Chen, Y. Kurata, S. Isoda. Small **3**, *8*, 1356 (2007).
[28] R.M. Cornell, U. Schwertmann. The Iron Oxides: Structure, Properties, Reactions, Occurrences and Uses, Chapt. 2, Crystal Structure, 2nd Ed.; Wiley-VCH Publishers, Weinheim, Germany (2003).
[29] M. Murayama, J.M. Howe, H. Hidaka, S. Tanaki. Science **295**, 2433 (2002).
[30] V. Shukla. Nanoscale Adv. **1**, *5*, 1640 (2019).
[31] G. Sun, B. Dong, M. Cao, B. Wei, C. Hu. Chem. Mat. **23**, 1587 (2011).
[32] G. Liu, L. Wang, Z. Yang, R. Wu. J. Alloys Compd. **718**, 46 (2017).

Translated by M.Verenikina